

Rupture of wet mantle wedge by self-promoting carbonation

Atsushi Okamoto ^{1✉}, Ryosuke Oyanagi ^{2,3}, Kazuki Yoshida¹, Masaaki Uno ¹, Hiroyuki Shimizu⁴ & Madhusoodhan Satish-Kumar ⁵

More than one teramole of carbon per year is subducted as carbonate or carbonaceous material. However, the influence of carbonation/decarbonation reactions on seismic activity within subduction zones is poorly understood. Here we present field and microstructural observations, including stable isotope analyses, of carbonate veins within the Higuchi serpentinite body, Japan. We find that the carbon and oxygen isotope compositions of carbonate veins indicate that carbonic fluids originated from organic materials in metasediments. Thermodynamic calculations reveal that carbonation of serpentinite was accompanied by a solid volume decrease, dehydration, and high magnesium mobility. We propose that carbonation of the mantle wedge occurs episodically in a self-promoting way and is controlled by a solid volume contraction and fluid overpressure. In our conceptual model, brittle fracturing and carbonate precipitation were followed by ductile flow of carbonates and hydrous minerals; this might explain the occurrence of episodic tremor and slip in the serpentinized mantle wedge.

¹Graduate School of Environmental Studies, Tohoku University, Sendai, Japan. ²Research Institute for Marine Geodynamics, Japan Agency for Marine-Earth Science and Technology (JAMSTEC), Yokosuka, Japan. ³School of Science and Engineering, Kokushikan University, Tokyo, Japan. ⁴Geotechnical Analysis Group, Advanced Analysis Department, Civil Engineering Design Division, Kajima Corporation, Tokyo, Japan. ⁵Faculty of Science, Department of Geology, Niigata University, Niigata, Japan. ✉email: atsushi.okamoto.d4@tohoku.ac.jp

Subduction zones transport surface materials deep into Earth's interior. Metamorphism of subducted lithosphere releases water and CO₂ to the overlying accretionary prism or mantle wedge^{1–6}. Subduction zone fluids contain various chemical species and have a wide range of pH that varies in response to *P–T* conditions^{7–9}. Large gradients in temperature and chemical potential along the subduction interface generate ideal conditions for mineral dissolution, precipitation, and metasomatism^{4,10–12}. Such chemical reactions can change mechanical strength, permeability, and fluid pressure, and thus influence the rheological and seismological characteristics of subduction zones¹⁰. For example, silica precipitation may control the recurrence periods of ordinary earthquakes¹³ and slow earthquakes within subduction zones¹⁴.

Along the slab–mantle interface below the forearc Moho, hydration of mantle peridotite forms serpentine minerals and hydrous metasomatic minerals such as talc, amphibole, phlogopite, and chlorite^{4,10,15–18}. Hydration can lower fluid pressure, and the plastic flow or frictional sliding of hydrous minerals result in steady-state slip¹⁸. Therefore, the downdip limit of large earthquakes (seismogenic zone) can be defined either by the brittle–ductile transition in crustal rocks (i.e., 350–400 °C) or the intersection of the subduction thrust and the forearc Moho^{10,19}. Slow slip events (SSEs) are observed at depths corresponding to the transition between the seismogenic zone and the deeper stably sliding zone^{20–23}. Slow slip events include long-term slip events that occur in relatively shallow parts of the subduction interface, and episodic tremor and slip (ETS) in relatively deep parts. In warm subduction zones such as Nankai and northern Cascadia, ETS is abundant in the corner of the mantle wedge^{20–23}, a region that could be dominated by serpentinite formed by fluids released from the subducting slab. Several geological models involving chemical reactions have been proposed to explain ETS, including those that involve silica precipitation^{14,24} and the formation of serpentine–brucite assemblages²⁵, and dehydration-induced heterogeneity within eclogitic oceanic crust²⁶. Metasomatic reaction between ultramafic rocks and crustal rocks has been proposed as a mechanism to explain ETS²⁷. Because most metasomatic reactions that occur in serpentinitized mantle release liquid water^{10,12,27}, mechanical instabilities might be generated by fluid overpressure. However, the build-up of fluid overpressure is controlled by various factors including the relative rates of fluid generation, pore generation, and pore collapse^{28,29}, and the geological mechanisms controlling the interplay between these factors in the ETS source region remain debated.

Estimates of the carbon budget in subduction zones suggest that more than one teramole of carbon is subducted each year as carbonates or carbonaceous materials^{1,2,30}. The nature of carbon-bearing fluids (e.g., carbon dioxide, methane) and their interaction with rocks are highly sensitive to redox conditions³¹. Graphite has been considered as a sink of carbon within the subducting slab due to its low solubility in fluids³¹. However, recent experimental and thermodynamic modeling studies have revealed that graphite solubility is enhanced by pH and dissolved silica³², and that the dissolution of carbonaceous materials in sediments plays an essential role in generating carbon-bearing fluids in subduction zones³³. Carbon-bearing fluids are also produced by the decomposition of carbonates via infiltration of H₂O-rich fluids^{1,2,5} and by fluid-induced dissolution of carbonate minerals coupled with precipitation of silicate minerals¹¹. In particular, mantle peridotite has the potential to influence deep carbon cycling by acting as a voluminous sink of CO₂. Carbonation of exhumed oceanic mantle and carbon storage within ophicarbonates are commonly reported³⁴, whereas the behavior of carbon-bearing fluids in subduction-related serpentinites is more complex^{35–39}. When carbonates are in contact

with serpentinite, graphite is often formed due to the relatively reducing conditions associated with serpentinite^{35,36}. In contrast, reports of high-pressure carbonated serpentinites related to subduction zones^{37–39} highlight the potential for long-term CO₂ sequestration in the subducting slab and mantle wedge, even although some studies suggest that most subducted carbonate is recycled back to the surface⁵. In addition, carbonation and decarbonation reactions can induce changes to the mechanical properties of mantle rocks. For example, infiltration of reducing fluids can promote strain localization in carbonated serpentinites, implying that carbonic fluids could have an influence on earthquake processes in subduction zones³⁶. Experiments involving in situ carbonation of antigorite indicate volume contraction during this reaction⁴⁰. These results indicate that carbonation of mantle wedge potentially have effects on the behavior of subduction zone thrusts. However, our understanding of carbonation processes in the mantle wedge is limited by a lack of well-characterized examples from ancient exhumed subduction zones. Carbonated serpentinites from the high-pressure (*HP*) Sanbagawa metamorphic belt in Japan, which represents part of an exhumed Cretaceous subduction zone, provide an unique opportunity to understand the mechanisms of carbonation within a mantle wedge corner under *P–T* conditions similar to those at which active ETS is reported.

Results and discussion

Carbonation of serpentinite associated with brittle fracturing.

The Sanbagawa belt is a *HP* metamorphic belt that extends ~800 km along the Median Tectonic Line from the Kanto Mountains in the east to Kyushu in the west along Japan (Supplementary Fig. 1)⁴¹. It is composed mainly of metasediments and metabasalts that formed during Cretaceous subduction of an oceanic plate. The metamorphic belt also contains meter- to kilometer-scale ultramafic blocks including mantle peridotites, serpentinites, and tremolite-rich rocks⁴². The mineral compositions and restricted distribution of these ultramafic blocks to regions higher than chlorite zone indicate that they originated in the mantle wedge^{25,42,43}. The Higuchi serpentinite body (15 × 8 m; Fig. 1a) is located in the Kanto Mountains near the boundary between the garnet and chlorite zones (36°07′30.7″N 139°07′00.0″E; Supplementary Fig. 1). Raman analysis of carbonaceous materials indicates peak temperatures of 400–450 °C in this area⁴⁴, and mineral phase equilibria suggest peak pressures of ~0.5–0.9 GPa⁴⁵. The long axis of the serpentinite body is subparallel to a mineral lineation in the surrounding pelitic schists. The Higuchi body is composed of massive or foliated antigorite (Fig. 1b, c) that is cut by dense networks of multi-generational carbonate(s) + talc veins (Fig. 1a–e and Supplementary Fig. 2), including magnesite (Fig. 1c, d), dolomite (Fig. 1a, b), and dolomite + calcite (Fig. 1e). The carbonate veins propagate from the margin to the center of the body in a branching network (Supplementary Fig. 2). Along contacts with serpentinite (Fig. 1f), the pelitic schists are progressively converted to layers of chlorite rock ~50 cm wide that preserve bands containing primary metamorphic graphite, and then to lenses of actinolite + chlorite schist up to ~30 cm wide (Supplementary Fig. 3).

Blocks of massive serpentinite (Fig. 1b) are composed of randomly oriented antigorite grains (Fig. 2a, b) with minor amounts of Cr-rich spinel. Olivine, pyroxenes, and brucite are absent. Cr-rich spinel is commonly altered to magnesiochromite (Fig. 2c and Supplementary Table 1), but some Cr-rich spinel grains in the serpentinite and actinolite–chlorite schists retain unaltered cores with X_{Cr} (= Cr/(Cr+Al)) = 0.52–0.58 and X_{Mg} (= Mg/(Mg+Fe)) = 0.55–0.64. Such depleted spinel compositions in the Higuchi serpentinite are similar to those in forearc

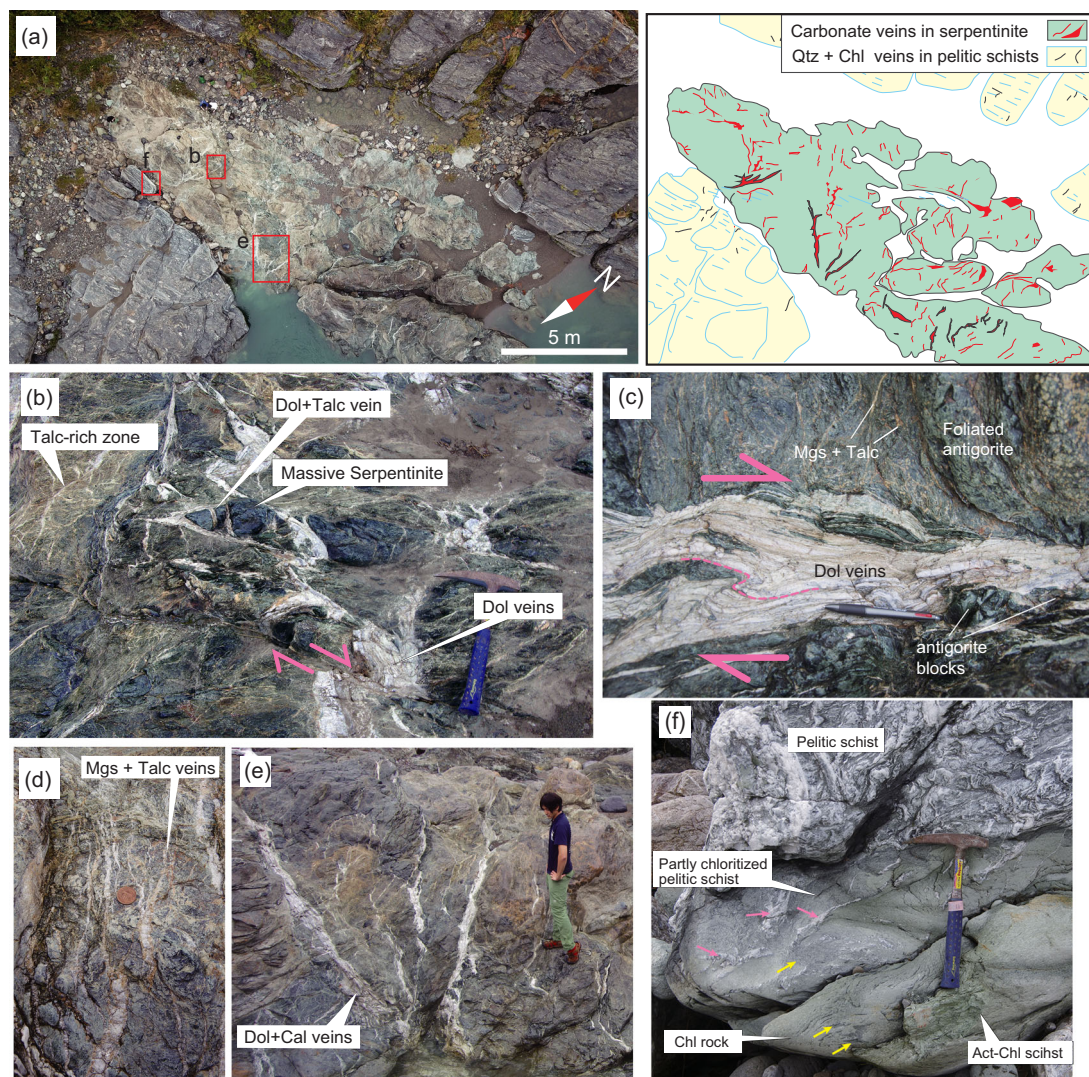


Fig. 1 Field characteristics of the carbonated serpentinite body in Higuchi, Sanbagawa belt, Japan. **a** Drone photograph and schematic illustration (at right) of the Higuchi serpentinite body with carbonate veins. Open rectangles indicate the locations of **b**, **f**, and **e**, respectively. **b** Dolomite veins cut through massive serpentinite blocks. **c** Layered dolomite veins that have experienced shear deformation. **d** Magnesite + talc veins. **e** Thick dolomite + calcite veins associated with fragments of serpentinite blocks. **f** Chlorite rock and actinolite-chlorite schist at the boundary between pelitic schist and the Higuchi serpentinite body. Yellow and pink arrows indicate relict bands of graphite and quartz-rich material, respectively. Mgs magnesite, Dol dolomite, Cal calcite, Chl chlorite, Act actinolite.

peridotites⁴⁶ and those of other ultramafic bodies in the Sanbagawa belt^{43,47} (Fig. 2c). Carbonate veins in the Higuchi body are composed mainly of dolomite and magnesite, with lesser amounts of calcite. Magnesite commonly occurs as patches 0.2–2.0 mm in size within antigorite blocks (Fig. 2a, d, e), often accompanied by networks of talc veins <1 mm thick. Magnesite–talc layers also occur along foliation surfaces (Fig. 2a), and infill the spaces between asymmetric antigorite blocks produced by brittle shear deformation (Fig. 2e). Dolomite + talc veins are the most distinct veins in the serpentinite body because they are relatively thick (>2 cm) and can be >3 m long (Figs. 1b, c and 2f). Talc occurs along the margins of these veins (Fig. 2f). Some thick dolomite veins show a layered structure including enclaves of serpentinite (Fig. 1b, c, e). The asymmetry of serpentine fragments, the presence of asymmetric folds (Fig. 1c), and the presence of several layers composed of dynamically recrystallized dolomite grains cutting coarse-grained dolomite veins (Fig. 2g), indicate that vein formation and development of localized shear zones was a repetitive process. In some relatively

thick veins, euhedral dolomite crystals grew in the center of the veins, and anhedral calcite crystals filled the intervening pore spaces (Fig. 2h). The dolomite crystals in contact with calcite have higher-Fe rims (Supplementary Fig. 4), suggesting that such dolomite rims were in equilibrium with calcite (Supplementary Table 1). Application of calcite–dolomite solvus thermometry⁴⁸ to these veins indicates a carbonation temperature of 380–400 °C (Supplementary Fig. 4).

Sources and compositions of carbonic fluids. Carbonic fluids in subduction zones are commonly sourced from carbonates in seafloor sediments, hydrothermal alteration of basaltic oceanic crust^{1,2,30}, or organic materials in sediments^{30,33}. In the Sanbagawa belt, the rare marbles have $\delta^{13}\text{C}$ values of 0.4–2.8‰, typical of marine limestones⁴⁹ (Fig. 2i). The stable isotope compositions of calcite in pelitic and basic schists, and related veins, have relatively constant $\delta^{18}\text{O}$ values (15–17‰) and a large variation in $\delta^{13}\text{C}$ (–12–2‰), reflecting multiple sources of CO_2 including oxidation of in situ biogenic carbonaceous material and

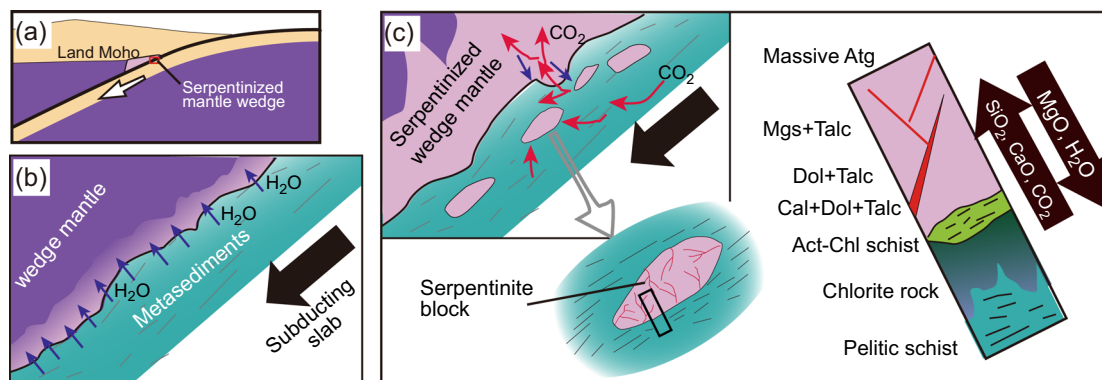


Fig. 3 Schematic illustration of carbonation in the mantle wedge. **a** Subduction zone setting at the leading edge of the mantle wedge. **b** Pervasive serpentinization at the leading edge of the mantle wedge is associated with the release of H₂O from the subducting slab. **c** Localized carbonation of serpentinized mantle wedge and serpentinite blocks associated with production of carbonic fluids.

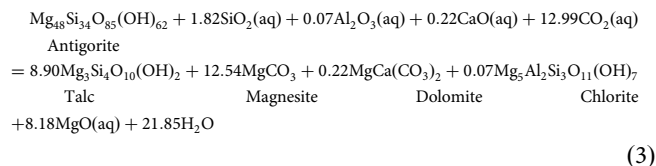
Progress of carbonation assisted by reaction-induced fracturing and Mg-mobility. We conducted thermodynamic modeling of the interactions between pelite-derived fluids and serpentinite at 400 °C and 0.5 GPa with variable fluid–rock ratios (F/R ratio; see Methods section). The initial fluids were assumed to be in equilibrium with the graphite-bearing pelitic schists at various oxygen fugacities, f_{O_2} (Supplementary Fig. 6). Given graphite saturated fluids, the atomic fraction of oxygen to oxygen + hydrogen in initial fluid, X_O , is determined for each f_{O_2} ⁵³.

At 400 °C and 0.5 GPa, graphite-bearing assemblages appear at high F/R ratios when antigorite reacts with relatively reducing fluids (Fig. 4a). This is because the solubility of graphite decreases slightly with the addition of antigorite to reducing fluids, as the precipitation of clinopyroxene and tremolite reduces the concentration of Ca-bearing carbonic aqueous complexes, such as $Ca(HCOO)^+$, $Ca(HCO_3)^+$, and $CaCO_{3,aq}$. In cases with initial fluids at around the quartz–fayalite–magnetite (QFM) buffer ($f_{O_2} = -28.1$, $X_O = 0.337$), relatively common metasomatic minerals (tremolite, chlorite, talc)¹² appear along the interfaces between ultramafic rocks and metasediments at $\log [F/R]$ of 1.5–2.5.

Typical carbonate-bearing mineral assemblages are found in cases with initial fluids at around QFM + 0.3 ($f_{O_2} = -27.8$, $X_O = 0.344$; Fig. 4a, b). At $\log [F/R] > \sim 2.5$, plagioclase, calcite, chlorite, and quartz appear, which are typical minerals in veins within the Sanbagawa pelitic schists⁵⁴. With an increase in the proportion of antigorite, the mineral assemblage evolves as follows: $Chl \pm Qtz \pm Cpx/Chl + Tr/Cal + Talc/Dol + Talc/Mgs + Talc/Mgs + Talc + Atg$ (Fig. 4b, c). Such a mineralogical sequence reflects the fluid-dominated system at the boundary of the serpentinite body and close to the large veins, and the rock-dominated system in the interior of the serpentinite body with a fine vein network (Fig. 4c) observed within the Higuchi serpentinite body (Figs. 1–2). At $\log [F/R] < 2.0$, H₂O is released by tremolite, and talc and carbonates form at the expense of antigorite, while CO₂ is consumed (Fig. 4d). Carbonaceous material in sedimentary rocks is initially poorly crystalline, and its crystallinity increases during prograde metamorphism in subduction zones. Therefore, relatively disordered graphite exists in the metapelites around the Higuchi body⁴⁴. In the presence of disordered graphite, the CO₂ concentration in the input solution could have been greater than those estimated by our thermodynamic calculations (Fig. 4d), which assumed the presence of crystalline graphite³³. This could result in the formation of larger amounts of carbonates at the same f_{O_2} conditions in the initial solution.

With a decrease in the F/R ratio ($\log [F/R] < 1.5$; i.e., representative of the interior of the serpentinite body), carbonates + talc form by consumption of antigorite. pH increases and

f_{O_2} slightly decreases (Supplementary Fig. 7), as reported in previous studies^{35,36,55}. Si is the dominant component in the initial fluid, as it is saturated with quartz (Fig. 4e). The aqueous CO₂ species dominantly exists as the $MgOSi(OH)_2(HCO_3)^+$ complex (Supplementary Fig. 7). Such effects of SiO₂ on the enhancement of carbon solubility have been inferred from dissolution experiments on forsterite + enstatite + graphite³². As the amount of antigorite increases, the concentration of Si decreases and the concentration of Mg increases (Fig. 4e). For example, at $\log [F/R] = 1.0$, the overall mass balance for the carbonation of serpentinite is:



In reaction 3, a small amount of chlorite is formed. Chlorite is not found in the Higuchi serpentinite, but Al-rich antigorite often occurs with talc. Interestingly, the Mg concentration at low $[F/R]$ ($< \sim 1.5$), which exists dominantly as $Mg(OH)_2,aq$ (Supplementary Fig. 7), is higher than the Si concentration in the initial fluid, implying relatively high mobility of Mg in the mantle wedge. Moreover, at low F/R where talc + carbonates are formed (Fig. 4f), the solid volume decreases ($V_{solid}/V_{solid,0} = 0.7\text{--}1.0$), whereas the total volume (solid + fluid) increases ($V_{total}/V_{total,0} = 1.000\text{--}1.004$). Observations from recent laboratory experiments conducted under forearc mantle conditions⁴⁰ support our modeling and field observations, suggesting that the progressive formation of magnesite + talc is associated with a solid volume decrease. Although the fluid–mineral equilibria and volume changes were computed for isobaric condition (Fig. 4f), the values of $V_{total}/V_{total,0} > 1$ at low F/R suggest that carbonation reactions of serpentinized mantle tend to result in a fluid pressure rise when the system is undrained.

Fracturing induced by volume-changing reactions. To understand the effects of the solid volume change and fluid pressure increase on fracturing, we conducted numerical simulations of coupled fracturing, reaction, fluid flow, and element diffusion using a distinct element method⁵⁶ (see Methods section). We consider a simple metasomatic dehydration reaction between a serpentinite body and a matrix of pelitic schist (Fig. 5a), in the cases of dilation (Fig. 5b) and contraction (Fig. 5c). In the model, the reaction proceeds along the margins and fractures within the serpentinite body in response to diffusive flux of metasomatic agents (i.e., CO₂ species or silica), which is saturated in the pelitic

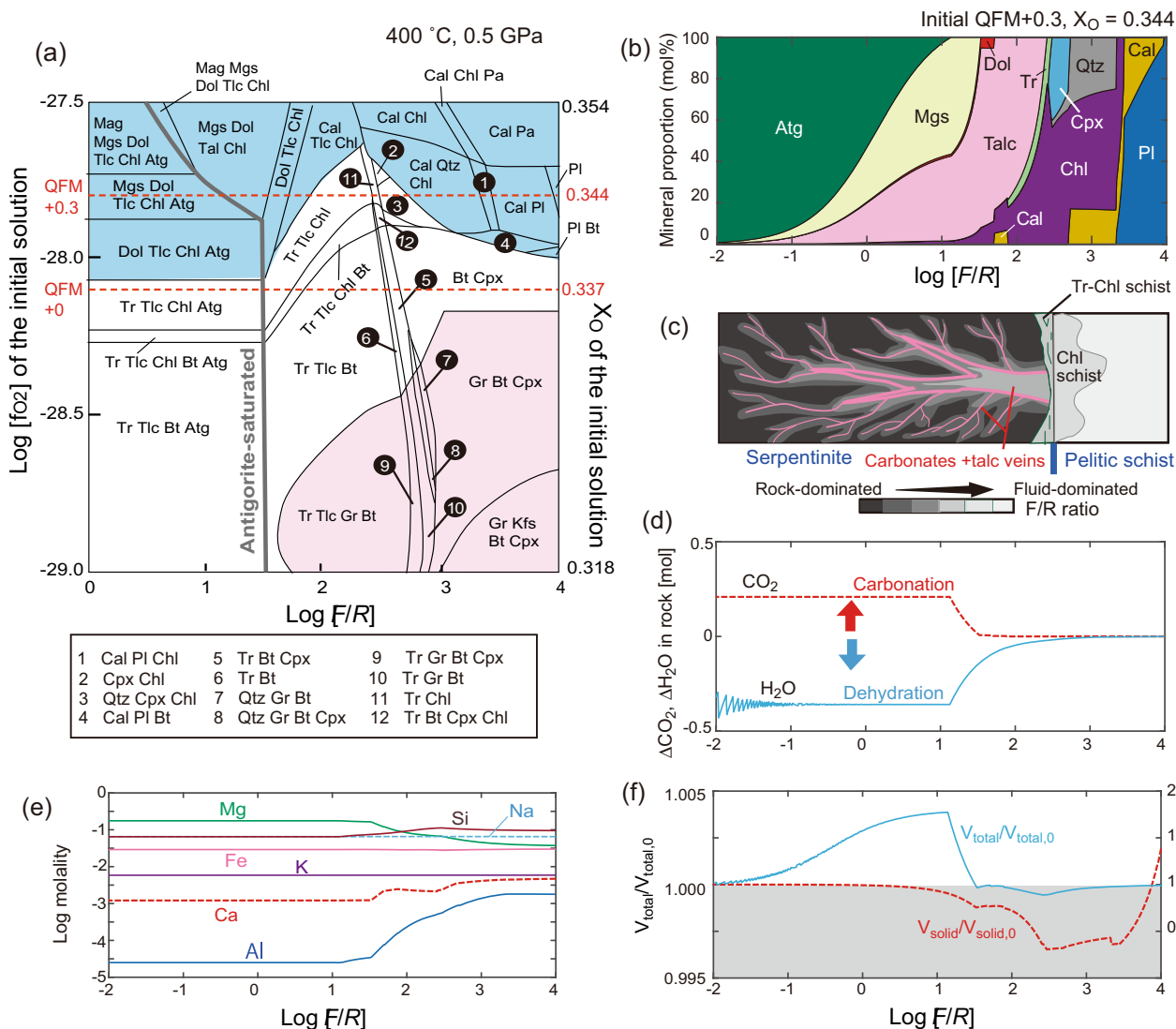


Fig. 4 Results of thermodynamic calculations of the interaction between pelitic-schist-derived fluids and antigorite at 400 °C and 0.5 GPa. **a** Stable mineral assemblage as a function of fluid/rock mass ratio (F/R) and oxygen fugacity, f_{O_2} and the atomic fraction of oxygen to oxygen + hydration, X_O , of the initial solution. Pale blue and pink shaded regions indicate carbonate- and graphite-bearing assemblages, respectively. Red dashed lines indicate QFM + 0 ($X_O = 0.337$) and QFM + 0.3 ($X_O = 0.344$) of the initial solution. **b–f** Results in the case of $\log f_{O_2} = -27.8$ (QFM + 0.3, $X_O = 0.344$) of the initial solution as a function of $\log [F/R]$. **b** Mole percent of product minerals. **c** Schematic illustration showing the relationship between the F/R ratio and mineralogical evolution of the Higuchi serpentinite body. **d** Change in moles of H_2O (ΔH_2O) and CO_2 (ΔCO_2) in rock before and after reaction. **e** Total concentration (mol/kg) of individual elements (Si, Al, Fe, Mg, Ca, Na, K) in fluids. **f** Solid volume ratio ($V_{solid}/V_{solid,0}$) and total volume ratio ($V_{total}/V_{total,0}$) before and after reaction. Kfs K-feldspar, Bt biotite, Cpx clinopyroxene, Tr tremolite, Chl chlorite, Qtz quartz, Cal calcite, Dol dolomite, Mgs magnesite, Gr graphite, Pl plagioclase, Pa paragonite, Mag magnetite.

schist. In both cases of dilation and contraction, fluid pressure increases within the serpentinite body, but different fracture patterns are produced depending on the volume change. In the case of dilation, radial cracks develop preferentially within the surrounding matrix (Fig. 5b, d and Supplementary Fig. 10a). In contrast, fracture networks are preferentially developed within the serpentinite body in the case of contraction (Fig. 5c, d and Supplementary Fig. 10b), and the fracture networks develop from the margin with branching-out structure, which shows a similar geometry as the carbonate veins in the Higuchi body (Fig. 1a–e and Supplementary Fig. 2). These contrasting fracture patterns are consistent with previous numerical simulations^{56–59} and laboratory experiments^{28,40,58}. Similar fracture patterns are also reproduced (Supplementary Fig. 11) even when fracturing is simulated in models of metasomatic reaction with dilation or contraction but without fluid flow and dehydration. The

thermodynamic calculations (Fig. 4) and DEM simulations (Fig. 5) indicate that volume contraction is likely to be the main cause of fracturing during carbonation. Euhedral dolomite grains that are interpreted to have grown in open space (Fig. 2i) indicate that fluid overpressures sustained open cracks, and could have assisted the propagation of fractures. Fluid overpressure could be built up when the rate of fluid production is greater than that of fluid escape through the pelitic schist⁶⁰. The permeability of the pelitic schist in the Sanbagawa belt is estimated to be $2.1 \times 10^{-20} \text{ m}^2$ under a confining pressure of 200 MPa⁶¹, and the porosity of the pelitic schist could be low and similar to that of chlorite schist in subduction zones (0.01%–0.2%)⁶². Such low porosity and permeability in the pelitic schist and the relatively high reaction rate of carbonation with dehydration (several [tens of] percent of carbonation from an antigorite block in a few days)⁴⁰ could result in fluid overpressure within the serpentinite body, as discussed in

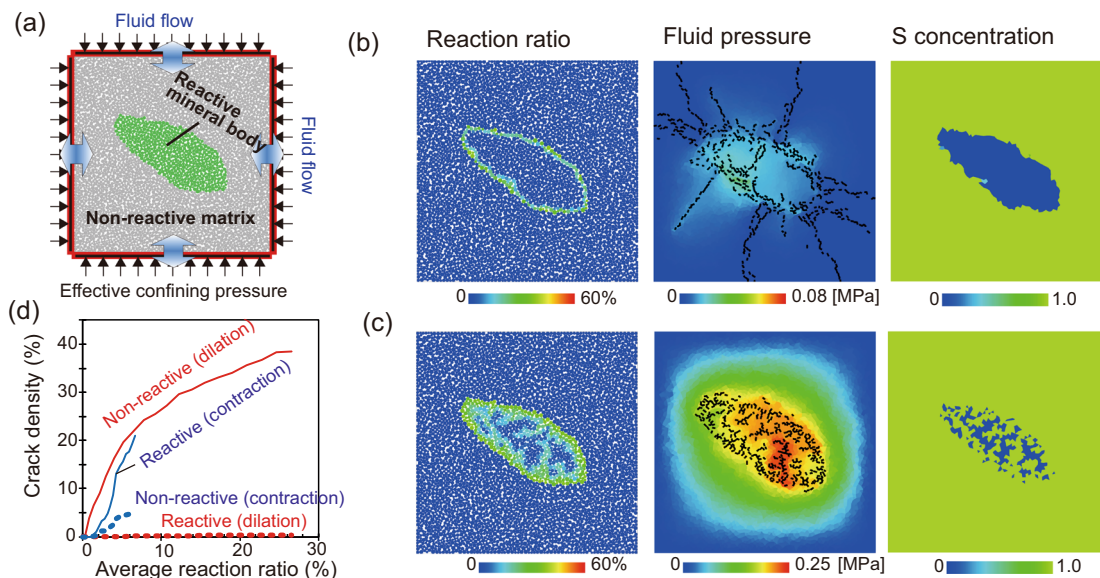


Fig. 5 Representative results of numerical simulations using distinct-element techniques of reaction-induced fracturing during carbonation of a serpentinite body in a non-reactive matrix. **a** Boundary conditions used in the model. **b, c** Snapshots of the reaction ratio (left), fluid pressure distribution ($P_f - P_{min}$) with the fracture pattern (middle) and the concentration of species *S* (right) during reaction progress. **b** Metasomatic dehydration with dilation at an average reaction ratio, $\xi_{Av} = 17.3\%$, and a volume strain $\varepsilon_v = 0.0076$; and **c** metasomatic dehydration with contraction at $\xi_{Av} = 5.5\%$, and the volume strain $\varepsilon_v = -0.005$. **d** The crack density (percentage of broken bonds with respect to total bonds) in the reactive material domain and non-reactive matrix for dilation and contraction reactions, respectively.

dehydration of serpentinite⁶⁰. The volume contraction produces tensile cracks at an isotropic effective confining stress (Fig. 5), but mechanical instabilities associated with volume changes and fluid overpressure during reaction can trigger earthquake ruptures at high differential stresses^{60,63}.

Consequences of heterogeneous and episodic carbonation in the mantle wedge. In the Sanbagawa belt, carbonation of some ultramafic blocks has occurred⁴⁷, but the distribution and extent of carbonation reactions are restricted^{40,47}. In the Higuchi body, carbonates were not formed during the initial stages of serpentinization (to form antigorite). These features suggest that in contrast to the relatively homogeneous serpentinization process (Fig. 3b), carbonation in the mantle wedge may involve rupturing that is heterogeneous in time and space (Fig. 3c). The reactions involving carbonic fluids are influenced by redox conditions. It is well known that peridotite has a high reducing potential^{64,65}, but the redox conditions in a fully serpentinized body could be modified by fluid–rock interactions after serpentinization⁶⁶. In the case of the Higuchi body, carbonation did not occur in the initial stage of serpentinization (massive antigorite; Fig. 2a, b), and chloritized pelitic schists at the boundary were not significantly depleted in graphite (Supplementary Figs. 3a and 5). Therefore, it is unlikely that the CO_2 fluid was produced only near the serpentinite body under oxidizing conditions. Based on analysis of the Higuchi body, we infer that carbonation of the mantle wedge can be induced by episodic ingress of carbonic fluids that may be created by oxidation of carbonaceous materials with fluids passing through subducted oxidized layers, including hematite-bearing mafic schists and bedded manganese deposits^{67,68}. In addition, we emphasize that once carbonic fluids reach the mantle wedge, carbonation can proceed in a self-promoting way via positive feedbacks between the reaction, volume contraction, fracturing, and transport of elements and CO_2 – H_2O fluids (Figs. 3–5)^{40,36}.

In the Nankai subduction zone in Shikoku, SW Japan, ETS is observed at the slab–mantle interface near the corner of the

mantle wedge^{20–23,69}. The frictional behavior of serpentinite, as well as metasomatic products such as talc, chlorite, and tremolite, is characterized by stable slip related to strain hardening⁷⁰. A notable feature of carbonation within the Higuchi body is that networks of millimeter- to meter-scale carbonate–talc veins developed during the carbonation of serpentinized mantle (Figs. 1–2 and Supplementary Fig. 2). The total volume increase (fluid + solid) suggested by the thermodynamic modeling of carbonation (Fig. 4f) might cause non-double coupled earthquakes, as reported in swarm seismicity in volcanic zones⁷¹. However, the signal of ETS is consistent with shear slip on the plate interface⁶⁹, and non-double coupled components are not clear due to the large signal-to-noise ratio. The high fluid pressure observed in the Higuchi body (Fig. 2) and suggested by the modeling (Fig. 4f) is consistent with high V_p/V_s ratios associated with the ETS region^{21,22}. The DEM modeling reveals that volume contraction in the presence of high fluid pressures tends to generate tensile fractures (Fig. 5 and Supplementary Fig. 10b), which may subsequently transform (or develop) into shear fractures under differential stress. The brittle shear failures observed in thin-sections and outcrops (Figs. 1b, c and 2e) are consistent with the mechanism of low-frequency earthquakes related to shear slip on the plate interface^{21,69}. Following sealing of void spaces by carbonates, localized shear is concentrated within the talc-rich layers (Figs. 1b and 2a, e) and dolomite veins (Figs. 1c and 2f). We speculate that this kind of repeated brittle failure, followed by viscous flow, may represent an analog for the ETS that is observed within the relatively cold nose of the mantle wedge.

Methods

Measurements of stable isotope compositions of carbonate minerals. The chemical compositions of minerals were analyzed using an electron microprobe analyzer (EPMA, JEOL8200) at Tohoku University. The acceleration voltage was 15 kV, and the current was 12 nA or 120 nA for quantitative analyses and elemental mapping, respectively. Identification of serpentinite and other minerals was performed using a Raman spectrometer (Horiba XploRa) equipped with an Olympus BX51 microscope at Tohoku University.

Oxygen ($\delta^{18}\text{O}$) and carbon ($\delta^{13}\text{C}$) isotope analyses were conducted on selected carbonate samples from the Higuchi serpentinite body. For comparison, we also analyzed the stable isotope compositions of marble samples from the Sanbagawa belt in central Shikoku. Samples were extracted from cut and polished slabs using a sharp knife, and then stained with Alizarin red-S to distinguish between calcite and dolomite. Staining with Alizarin red-S does not affect the C and O isotope ratios⁴⁹. Sample powders for C–O isotope analyses were taken from different portions of each slab. Carbonate mineral (dolomite, magnesite, or calcite) powders were placed in small stainless steel thimbles and dropped into a reaction vessel containing pyrophosphoric acid at 60 °C (calcite) or 100 °C (for dolomite and magnesite) in vacuum to produce CO₂ gas. Released CO₂ gas was cleaned to remove impurities like H₂O by using pentane slush and collected by using liquid nitrogen cold traps. Stable isotope measurements were carried out with a Thermofischer MAT-253 mass spectrometer at Niigata University. Results are reported in conventional per mil (‰) notation with respect to V-SMOW (Vienna-Standard Mean Ocean Water) for oxygen and V-PDB (Vienna-Peedee Belemnite) for carbon. The precision of $\delta^{13}\text{C}$ and $\delta^{18}\text{O}$ for the laboratory standard CO₂ gas were 0.04‰ and 0.06‰, respectively⁷².

Thermodynamic model of fluid–rock interaction. Thermodynamic calculations were carried out in the system Na–K–Ca–Fe–Mg–Al–Si–Cl–C–O–H using the Deep Earth Water (DEW) model^{73,74} and software EQ3/6⁷⁵ with a modified Berman thermodynamic dataset⁷⁶. This updated thermodynamic dataset includes H₂CO₃⁰, HCO₃[−], and various complexes related to bicarbonic acid (Na(HCO₃)⁰, Ca(HCO₃)⁺, and MgOSi(OH)₂(HCO₃)⁺). For this reason, thermodynamic calculations are not restricted to the H₂O-rich system but also model CO₂-rich fluids involving carbonation⁷⁴. We treated solid solutions as ideal mixing between Mg and Fe endmembers for chlorite, talc, tremolite, biotite, and clinopyroxene, and between albite and anorthite for plagioclase. We first created an input solution using EQ3, in equilibrium with the observed mineral assemblage in the pelitic schists: muscovite + chlorite ($X_{\text{Mg}} = 0.6$) + quartz + albite + clinozoisite + calcite + graphite, at 400 °C and 0.5 GPa^{34,77}. This mineral assemblage represents the most likely fluid source or the metasomatic and carbonation reactions within the serpentinite. The pressure of carbonation in the Higuchi serpentinite was not determined, but probably ranges between 0.5 and 0.9 GPa based on the *P*–*T* conditions in the chlorite and garnet zones⁴⁵. At 400 °C, there is no miscibility of CO₂–H₂O fluids below 1 GPa⁷⁸. The log oxygen fugacity of the input solutions, $\log[f_{\text{O}_2}]$, ranged from −29.0 to −27.5, corresponding to ΔQFM (deviation from quartz–fayalite–magnetite buffer) from −0.8 to +0.7 in log units⁷⁹. Based on the compositions of each initial solution calculated by EQ3, X_{O} is obtained as follows:

$$X_{\text{O}} = \frac{n_{\text{O}}}{n_{\text{O}} + n_{\text{H}}} \quad (4)$$

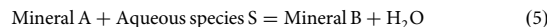
where n_{O} and n_{H} are the number of moles of oxygen and hydrogen in the fluids, respectively⁵³. The $\log[f_{\text{O}_2}]$ range of the initial solution corresponds to X_{O} from 0.318 to 0.354. EQ6 was then used to model the interactions (thermodynamic equilibria) between the input solution and serpentinite composed of 100% antigorite (Fig. 4). We calculated log fluid/rock mass ratios from −2.0 to 4.0. To create the stable mineral assemblage at various *F/R* and f_{O_2} conditions for the input solution (Fig. 4a and Supplementary Fig. 6), a shell script was written to automatically generate EQ3/6 run input files with various f_{O_2} conditions, and the output files generated by EQ3/6 were further processed with an author-generated MATLAB[®] script.

The changes in CO₂ and H₂O during the reactions (Fig. 4d) are calculated by determining changes in hydrous minerals and carbonates. The volume change ratio of the solids ($V_{\text{solid}}/V_{\text{solid},0}$; Fig. 4f) was calculated by using the volumes of product minerals and consumed antigorite. The volume change ratio of solid and fluids ($V_{\text{total}}/V_{\text{total},0}$) was calculated by the volumes of product minerals, consumed antigorite, and changes in the amount of fluid. The molar volume of fluids was obtained based on the sum of the concentration of carbonic species. With decreasing $\log[F/R]$, the X_{CO_2} values decreases from 2.30×10^{-2} to 1.88×10^{-2} .

We also undertook the same calculation at 400 °C and 1.0 GPa (Supplementary Fig. 8). We found that the topography of the stable mineral assemblage in a plot of $\log[f_{\text{O}_2}]$ vs. $\log[F/R]$ is largely similar to the case at 400 °C and 0.5 GPa (Fig. 4a), except that aragonite is stable instead of calcite. The chemistry of the initial solution calculated by EQ3 is also largely consistent with that calculated by Perple_X version 6.9.1.⁸⁰ with thermodynamic data of Holland and Powell⁸¹ (Supplementary Fig. 9).

Distinct element method to model metasomatic dehydration reactions. We conducted two-dimensional distinct-element numerical simulations to investigate fracture patterns induced by volume-changing dehydration reactions, following the methods of Okamoto & Shimizu⁵⁶ with slight modifications to incorporate element diffusion. Okamoto & Shimizu⁵⁶ treated coupled processes of reaction (dehydration/hydration), fluid flow, and fracturing. The model consists of an aggregate of circular elements connected by elastic bonds. When the external force exceeds the tensile or shear strength of the bond, the bond is broken to form a microcrack. To treat fluid flow, we calculate the fluid pressure in each domain, which is defined by the regions surrounded by connected elements. The fluid flow in a channel is calculated by the Poiseuille equation and includes the crack aperture (w), fluid viscosity (μ), the length of the flow channel, and the fluid pressure gradient

between adjacent domains (ΔP). Okamoto & Shimizu⁵⁶ considered a simple hydration/dehydration reaction as Mineral A + H₂O = Mineral B, and the reaction rate is assumed to be a linear function of fluid pressure. They showed that contrasting fracture patterns are produced in response to solid volume changes rather than fluid pressure as similar to the other studies^{56–59}. Here, as a simplification of the carbonation of serpentinite, we consider a simple metasomatic dehydration reaction:



where aqueous species S represents metasomatic agents such as CO₂ species and SiO₂. The reaction is characterized by the volume change factor (the volumetric ratio of 100% reacted particle to unreacted particle), the ratio of the changes in fluid and particle volume (fluid volume factor), and the ratio of the changes in the amount of species S with respect to the particle volume change (solute factor). For this study, we used volume factors of 1.1 (dilation) or 0.9 (contraction), a fluid factor of −0.1, and a solute factor of 1.0. The reaction rate, *Z*, is defined as a function of the concentration of C_s as follows:

$$Z = Z_{\text{max}}(1 - (C_{\text{s,max}} - C_{\text{s}})/(C_{\text{s,max}} - C_{\text{s,min}})) \quad (6)$$

$C_{\text{s,max}}$ and $C_{\text{s,min}}$ represent maximum and minimum concentrations of the species S in the system: the reaction rate is greatest (Z_{max}) at $C_{\text{s}} = C_{\text{s,max}}$, and the reaction stops at $C_{\text{s}} = C_{\text{s,min}}$. In addition to advective transport with H₂O, we consider diffusional transport of aqueous species S as a function of the concentration gradient of S in each domain.

The values of the parameters used in this study are summarized in Supplementary Table 3. This study used a 10 × 10 m square rock model that contains 4357 particles with diameters of 50–100 μm. This rock specimen initially contains a reactive mineral domain composed of antigorite (analogous to serpentinitized mantle) and a non-reactive matrix composed of quartz (analogous to metasediment). Here we consider that the species S is saturated within the non-reactive matrix. The physical properties (particle density, ρ , and Young's modulus, *E*) of the matrix material are based on quartz ($\rho = 2650 \text{ kg/m}^3$; $E = 140 \text{ GPa}$), whereas the reactive mineral properties change from antigorite ($\rho = 2600 \text{ kg/m}^3$; $E = 115 \text{ GPa}$) to a mixture of dolomite (95%) + talc (5%) ($\rho = 2830 \text{ kg/m}^3$; $E = 110 \text{ GPa}$), following the data of Mavko et al.⁸² and Abers & Hacker⁸³ (Supplementary Table 3). There are no experimental data on the tensile and shear strengths of these minerals, but the tensile strength of rock typically ranges from ~1 to 40 MPa, and compressive strengths are typically ~10 times the tensile strengths⁸⁴. Here, we set the tensile and shear strengths in the rock model to be 10 and 100 MPa, respectively, regardless of the minerals in the model. Based on these strength data, we performed preliminary simulations of uniaxial compression and tension tests to adjust microscopic input parameters⁸⁵, and decided to use a tensile spring strength of 30 MPa and a shear spring strength of 118 MPa. The effective confining pressure was set to be 1 MPa. The initial and fluid pressures outside the rock model were set to P_{min} , and when dehydration reaction proceeds fluid pressure, P_{f} inside the rock increases and fluid flows toward outside. The fluid physical properties (viscosity of $1.0 \times 10^{-4} \text{ Pas}$ and bulk modulus of 3.5 GPa) were assumed to be the same as those of water at temperatures of ~400 °C and pressures of 0.5 GPa. The concentration of species S, C_{s} , is assumed to be a maximum value ($C_{\text{s,max}} = 1.0$) in the non-reactive matrix (saturated), and C_{s} in the reactive mineral domain is set to be $C_{\text{s,min}}$ (=0) at the initial stage. The apparent diffusion coefficient (=diffusion coefficient/average particle size) was set to 0 s^{-1} in unbroken rocks, and 10 s^{-1} along fractures. As the diffusive flux of species is large with respect to the fluid flow, the concentration of S is nearly equal to $C_{\text{s,max}}$.

Reporting summary. Further information on research design is available in the Nature Research Reporting Summary linked to this article.

Data availability

The data of this study are available in methods and supplementary tables. The input and output files for EQ3 and EQ6 for representative cases (Fig. 4), and animations of the DEM simulation results are available in the online repository (<https://doi.org/10.6084/m9.figshare.13336850>).

Code availability

The DEM code used in this study is available from the corresponding author upon request with the approval of A.O. and H.S.

Received: 11 December 2020; Accepted: 13 July 2021;
Published online: 03 August 2021

References

- Kerrick, D. M. & Connolly, J. A. D. Metamorphic devolatilization of subducted oceanic basalts: implications for seismicity, arc magmatism and volatile recycling. *Earth Planet. Sci. Lett.* **189**, 19–29 (2001).

2. Kerrick, D. M. & Connolly, J. A. D. Metamorphic devolatilization of subducted marine sediments and the transport of volatiles into the Earth's mantle. *Nature* **411**, 293–296 (2001).
3. Hacker, B. R., Peacock, S. M., Abers, G. A. & Holloway, S. D. Subduction factory 2. Are intermediate-depth earthquakes in subducting slabs linked to metamorphic reactions? *J. Geophys. Res. Solid Earth* **108**, 2030 (2003).
4. Hyndman, R. D. & Peacock, S. M. Serpentinization of the forearc mantle. *Earth Planet. Sci. Lett.* **212**, 417–432 (2003).
5. Stewart, E. M. & Ague, J. J. Pervasive subduction zone devolatilization recycles CO₂ into the forearc. *Nat. Commun.* **11**, 6220 (2020).
6. Schmidt, M. & Poli, S. Experimentally based water budgets for dehydrating slabs and consequences for arc magma generation. *Earth Planet. Sci. Lett.* **163**, 361–379 (1998).
7. Manning, C. E. The chemistry of subduction-zone fluids. *Earth Planet. Sci. Lett.* **223**, 626 (1994).
8. Galvez, M. E., Connolly, J. A. D. & Manning, C. E. Implications for metal and volatile cycles from the pH of subduction zone fluids. *Nature* **359**, 420–424 (2016).
9. Scambelluri, M., Cannao, E. & Gilio, M. The water and fluid-mobile element cycles during serpentine subduction. A review. *Eur. J. Mineral.* **31**, 405–428 (2019).
10. Peacock, S. M. & Hyndman, R. D. Hydrous minerals in the mantle wedge and the maximum depth of subduction thrust earthquakes. *Geophys. Res. Lett.* **26**, 2517–2520 (1999).
11. Ague, J. J. & Nicolescu, S. Carbon dioxide released from subduction zones by fluid-mediated reactions. *Nat. Geosci.* **7**, 355–359 (2014).
12. Manning, C. E. Phase-equilibrium controls on SiO₂ metasomatism by aqueous fluid in subduction zones: reaction at constant pressure and temperature. *Int. Geol. Rev.* **37**, 1074–1093 (2015).
13. Saishu, H., Okamoto, A. & Otsubo, M. Silica precipitation potentially controls earthquake recurrence in seismogenic zones. *Sci. Rep.* **7**, 13337 (2017).
14. Audet, P. & Bürgmann, R. Possible control of subduction zone slow-earthquake periodicity by silica enrichment. *Nature* **510**, 389–392 (2014).
15. Fumagalli, P. & Poli, S. Experimentally determined phase relations in hydrous peridotites to 6.5 GPa and their consequences on the dynamics of subduction zones. *J. Petrol.* **46**, 555–578 (2005).
16. Fumagalli, P., Zanchetta, S. & Poli, S. Alkaline in phlogopite and amphibole and their effects on phase relations in metasomatized peridotites: a high-pressure study. *Contrib. Mineral. Petrol.* **158**, 723–737 (2009).
17. Tumiati, S., Fumagalli, P., Tiraboschi, C. & Poli, S. An experimental study on COH-bearing peridotite up to 3.2 GPa and implications for crust-mantle recycling. *J. Petrol.* **54**, 453–479 (2013).
18. Hirauchi, K., Katayama, I., Uehara, S., Miyahara, M. & Takai, Y. Inhibition of subduction thrust earthquakes by low-temperature plastic flow in serpentine. *Earth Planet. Sci. Lett.* **295**, 349–357 (2010).
19. Oleskevich, D. A., Hyndman, R. D. & Wang, K. The updip and downdip limits to great subduction earthquakes: thermal and structural models of Cascadia, south Alaska, SW Japan, and Chile. *J. Geophys. Res. Solid Earth* **14**, 14965–14991 (1999).
20. Beroza, G. C. & Ide, S. Slow earthquakes and nonvolcanic tremor. *Annu. Rev. Earth Planet. Sci.* **39**, 271–296 (2011).
21. Shelly, D. R., Beroza, G. C., Ide, S. & Nakamura, S. Low-frequency earthquakes in Shikoku, Japan, and their relationship to episodic tremor and slip. *Nature* **442**, 188–191 (2006).
22. Kato, A. et al. Variations of fluid pressure within the subducting oceanic crust and slow earthquakes. *Geophys. Res. Lett.* **37**, L14310 (2010).
23. Gao, X. & Wang, K. Rheological separation of the megathrust seismogenic zone and episodic tremor and slip. *Nature* **543**, 416–419 (2010).
24. Ujiie, K. et al. An explanation of episodic tremor and slow slip constrained by crack-seal veins and viscous shear in subduction mélange. *Geophys. Res. Lett.* **45**, 5371–5379 (2019).
25. Mizukami, T. et al. Two types of antigorite serpentine controlling heterogeneous slow-slip behaviors of slab-mantle interface. *Earth Planet. Sci. Lett.* **401**, 148–158 (2014).
26. Behr, W. M., Kotowski, A. J. & Ashley, K. T. Dehydration-induced rheological heterogeneity and the deep tremor source in warm subduction zones. *Geology* **46**, 475–478 (2018).
27. Tarling, M. S., Smith, S. A. F. & Scott, J. M. Fluid overpressure from chemical reactions in serpentine within the source region of deep episodic tremor. *Nat. Geosci.* **12**, 1034–1042 (2019).
28. Miller, S. A., van der Zee, W., Olgaard, D. L. & Connolly, J. A. D. A fluid-pressure feedback model of dehydration reactions: experiments, modeling, and application to subduction zones. *Tectonophysics* **370**, 241–251 (2003).
29. Connolly, J. A. D. Devolatilization-generated fluid pressure and deformation-propagated fluid flow during prograde regional metamorphism. *J. Geophys. Res.* **102**, 18149–18173 (1997).
30. Kelemen, P. B. & Manning, C. E. Reevaluating carbon fluxes in subduction zones, what goes down, mostly comes up. *Proc. Natl. Acad. Sci. USA* **112**, E3997–E4006 (2014).
31. Galvez, M. E., Manning, C. E., Connolly, J. A. D. & Rumble, D. The solubility of rocks in metamorphic fluids: a model for rock-dominated conditions to upper mantle pressure and temperature. *Earth Planet. Sci. Lett.* **430**, 486–498 (2015).
32. Tumiati, S. et al. Silicate dissolution boosts the CO₂ concentrations in subduction fluids. *Nat. Commun.* **8**, 16 (2017).
33. Tumiati, T. et al. Dissolution susceptibility of glass-like carbon versus crystalline graphite in high-pressure aqueous fluids and implications for the behavior of organic matter in subduction zones. *Geochim. Cosmochim. Acta* **273**, 383–402 (2020).
34. Kelemen, P. B. & Matter, J. In situ carbonation of peridotite for CO₂ storage. *Proc. Natl. Acad. Sci. USA* **105**, 17295–17300 (2008).
35. Galvez, M. E. et al. Graphite formation by carbonate reduction during subduction. *Nat. Geosci.* **6**, 473–477 (2013).
36. Giuntoli, F., Brovarone, A. V. & Menegon, L. Feedback between high-pressure genesis of abiotic methane and strain localization in subducted carbonate rocks. *Sci. Rep.* **10**, 9848 (2020).
37. Peacock, S. M. Serpentinization and infiltration metasomatism in the Trinity peridotite, Klamath province, northern California: implications for subduction zones. *Contrib. Mineral. Petrol.* **95**, 95–70 (1987).
38. Scambelluri, M. et al. Carbonation of subduction-zone serpentine (high-pressure phiocarbonate; Ligurian Western Alps) and implications for the deep carbon cycling. *Earth Planet. Sci. Lett.* **441**, 155–166 (2016).
39. Peng, W. et al. Multistage CO₂ sequestration in the subduction zone: insights from exhumed carbonated serpentinites, SW Tianshan UHP belt, China. *Geochim. Cosmochim. Acta* **270**, 218–243 (2020).
40. Sieber, M. J., Yaxley, G. M. & Hermann, J. Investigation of fluid-driven carbonation of a hydrated, forearc mantle wedge using serpentine cores in high-pressure experiments. *J. Petrol.* **61**, egaa035 (2020).
41. Wallis, S. R. & Okudaira, T. in *The Geology of Japan*. (eds T. Moreno, T., Wallis, S. R., Kojima, T. & Gibbons W.) 101–124. (Geological Society of London, 2016).
42. Aoya, M., Endo, S., Mizukami, T. & Wallis, S. R. Paleo-mantle wedge preserved in the Sambagawa high-pressure metamorphic belt and the thickness of forearc continental crust. *Geology* **41**, 451–454 (2013).
43. Hattori, K., Wallis, S., Enami, M. & Mizukami, T. Subduction of mantle wedge peridotites: evidence from the Higashi-Akaishi ultramafic body in the Sanbagawa metamorphic belt. *Isl. Arc* **19**, 192–207 (2010).
44. Inui, M. & Takefuji, A. Spatial distribution of garnet indicating control of bulk rock chemistry in the Sanbagawa metamorphic rocks, Kanto Mountains, Japan. *J. Mineral. Petrol. Sci.* **113**, 181–189 (2018).
45. Enami, M., Wallis, S. R. & Banno, Y. Paragenesis of sodic-pyroxene-bearing quartz schists: implications for the P–T history of the Sanbagawa belt. *Contrib. Mineral. Petrol.* **116**, 182–198 (1994).
46. Ishii, T., Robinson, P. T., Maekawa, H. & Fiske, R. Petrological studies of peridotites from diapiric serpentine seamments in the Izu-Ogasawara-Mariana forearc, Leg 125. In *Proc. Proceedings of the Ocean Drilling Program, Scientific Results, College Station, TX (Ocean Drilling Program)*. (eds Fryer P., Pearce J. A., Stokking L. B., et al.) 445–85 (1992).
47. Kawahara, H. et al. Brucite as an important phase of the shallow mantle wedge: evidence from the Shiraga unit of the Sanbagawa subduction zone, SW, Japan. *Lithos* **254–255**, 53–66 (2016).
48. Powell, R., Condliffe, D. M. & Condliffe, E. Calcite-dolomite geothermometry in the system CaCO₃-MgCO₃-FeCO₃: an experimental study. *J. Metamorph. Geol.* **2**, 33–41 (1984).
49. Wada, H., Enami, M. & Yanagi, T. Isotopic studies of marbles in the Sanbagawa metamorphic terrain, central Shikoku, Japan. *Geochem. J.* **18**, 61–73 (1984).
50. Morohashi, K., Okamoto, A., Satish-Kumar, M. & Tsuchiya, N. Variations in stable isotope compositions ($\delta^{13}\text{C}$, $\delta^{18}\text{O}$) of calcite within exhumation-related veins from the Sanbagawa metamorphic belt. *J. Mineral. Petrol. Sci.* **105**, 361–365 (2008).
51. Menzel, M. D. et al. Carbonation of mantle peridotite by CO₂-rich fluids: the formation of listwanites in the Advocate ophiolite complex (Newfoundland, Canada). *Lithos* **323**, 238–261 (2018).
52. Hansen, L. D. & Dipple, C. M. Carbonated serpentine (listwanite) at Atlin, British Columbia: a geological analogue to carbon dioxide sequestration. *Can. Mineral.* **43**, 225–239 (2005).
53. Connolly, J. A. D. Phase diagram methods for graphitic rocks and application to the system C-O-H-FeO-TiO₂-SiO₂. *Contrib. Mineral. Petrol.* **119**, 94–116 (1995).
54. Okamoto, A., Kikuchi, T. & Tsuchiya, N. Mineral distribution within polymetamorphic veins in the Sanbagawa belt, Japan: implications for mass transfer during vein formation. *Contrib. Mineral. Petrol.* **156**, 323–336 (2008).

55. Brovarone, A. V. et al. Subduction hides high-pressure sources of energy that may feed the deep subsurface biosphere. *Nat. Commun.* **11**, 3880 (2020).
56. Okamoto, A. & Shimizu, H. Contrasting fracture patterns induced by volume-increasing and -decreasing reactions: implications for the progress of metamorphic reactions. *Earth Planet. Sci. Lett.* **415**, 9–18 (2015).
57. Jamtveit, B., Malthe-Sørenssen, A. & Kostenko, O. Reaction enhanced permeability during retrogressive metamorphism. *Earth Planet. Sci. Lett.* **267**, 620–627 (2008).
58. Kuleci, H., Ulven, O. I., Rybacki, E., Wunder, B. & Abart, R. Reaction-induced fracturing in a hot pressed calcite-periclase aggregate. *J. Struct. Geol.* **94**, 116–135 (2017).
59. Yoshida, K., Okamoto, A., Shimizu, H., Oyanagi, R., Tsuchiya, N. & Oman Drilling Project Phase 2 Science Party. Fluid infiltration through oceanic lower crust in response to reaction-induced fracturing: Insights from serpentinized troctolite and numerical models. *J. Geophys. Res.* **125**, e2020JB020268 (2020).
60. Ague, J. J., Park, J. & Rye, D. M. Regional metamorphic dehydration and seismic hazard. *Geophys. Res. Lett.* **25**, 4221–4224 (1998).
61. Wibberley, C. A. J. & Shimamoto, T. Internal structure and permeability of major strike-slip fault zones: the Median Tectonic Line in Mie Prefecture, Southwest Japan. *J. Struct. Geol.* **25**, 59–78 (2003).
62. Ganzhorn, A. C., Pilorge, H. & Reynard, B. Porosity of metamorphic rocks and fluid migration within subduction interfaces. *Earth Planet. Sci. Lett.* **522**, 107–117 (2019).
63. Kirby, S. H., Durham, W. B. & Stern, L. A. Mantle phase changes and deep-earthquake faulting in subducting lithospheres. *Science* **252**, 216–225 (1991).
64. Klein, F. & Bach, W. Fe–Ni–Co–O–S phase relations in peridotite–seawater interactions. *J. Petrol.* **50**, 37–59 (2009).
65. Piccoli, F. et al. Subducting serpentinites release reduced, not oxidized, aqueous fluids. *Sci. Rep.* **9**, 19573 (2019).
66. Malvoisin, B., Chopin, C., Brunet, F. & Galvez, M. E. Low-temperature wollastonite formed by carbonate reduction: a marker of serpentinite redox conditions. *J. Petrol.* **53**, 159–176 (2012).
67. Nakagawa, M., Santosh, M. & Maruyama, S. Manganese formations in the accretionary belts of Japan: implications for subduction-accretion process in an active convergent margin. *J. Asian Earth Sci.* **42**, 208–222 (2011).
68. Tumiati, S., Godard, G., Matrin, S., Malaspina, N. & Poli, S. Ultra-oxidized rocks in subduction mélanges? Decoupling between oxygen fugacity and oxygen availability in a Mn-rich metasomatic environment. *Lithos* **226**, 116–130 (2015).
69. Ide, S., Shelly, D. R. & Beroza, G. C. Mechanism of deep low frequency earthquakes: Further evidence that deep non-volcanic tremor is generated by shear slip on the plate interface. *Geophys. Res. Lett.* **34**, L03308 (2007).
70. Hirauchi, K., den Hartog, S. A. M. & Spiers, C. J. Weakening of the slab–mantle wedge interface induced by metasomatic growth of talc. *Geology* **41**, 75–78 (2013).
71. Hrubcová, P., Doubravová, J. & Vavříček, V. Non-double-couple earthquakes in 2017 swarm in Reykjanes Peninsula, SW Iceland: sensitive indicator of volcano-tectonic movements at slow-spreading rift. *Earth Planet. Sci. Lett.* **563**, 116875 (2021).
72. Satish-Kumar, M., Kiran, S. & Abe, M. A new inlet system for microscale carbon and oxygen isotope analysis using dual inlet isotope ratio mass spectrometer at Niigata University, Japan. *Science Reports of Niigata University*. Vol. 35 (2021) (in press).
73. Sverjensky, D. A., Harrison, B. & Azzolini, D. Water in the deep Earth: The dielectric constant and the solubilities of quartz and corundum to 60kb and 1200°C. *Geochim. Cosmochim. Acta* **129**, 125–145 (2014).
74. Huang, F. & Sverjensky, D. A. Extended deep earth water for predicting major element mantle metasomatism. *Geochim. Cosmochim. Acta* **254**, 192–230 (2019).
75. Wolery T. J. EQ3NR, A Computer Program For Geochemical Aqueous Speciation–solubility Calculations: Theoretical Manual, User's Guide, And Related Documentation (version 7.0). (Lawrence Livermore National Laboratory, 1992).
76. Berman, R. G. Internally-consistent thermodynamic data for minerals in the system Na₂O–K₂O–CaO–MgO–FeO–Fe₂O₃–Al₂O₃–SiO₂–TiO₂–H₂O–CO₂. *J. Petrol.* **29**, 445–522 (1988).
77. Goto, A., Kunugiza, K. & Omori, S. Evolving fluid composition during prograde metamorphism in subduction zones: a new approach using carbonate-bearing assemblages in the pelitic system. *Gondwana Res.* **11**, 166–179 (2007).
78. Abramson, E. H., Bollengier, O. & Brown, M. The water–carbon dioxide miscibility surface to 450 °C and 7GPa. *Am. J. Sci.* **317**, 967–989 (2017).
79. Miozzi, F. & Tumiati, S. Aqueous concentration of CO₂ in carbon-saturated fluids as a highly sensitive oxybarometer. *Geochim. Perspect. Lett.* **16**, 30–34 (2020).
80. Connolly, J. A. D. Computation of phase equilibria by linear programming: a tool for geodynamic modeling and its application to subduction zone decarbonation. *Earth Planet. Sci. Lett.* **236**, 524–5412 (2005).
81. Holland, T. & Powell, R. An improved and extended internally consistent dataset for phases of petrological interest, involving a new equation of state for solid. *J. Metamorph. Geol.* **29**, 333–383 (2011).
82. Mavko, G., Mukerji, T. & Dvorkin, J. *The Rock Physics Handbook* (Cambridge University Press, 2009)
83. Abers, G. A. & Hacker, B. R. A MATLAB toolbox and excel workbook for calculating the densities, seismic wave speeds, and major element composition of minerals and rocks at pressure and temperature. *Geochem. Geophys. Geosyst.* **17**, 616–624 (2016).
84. Pollard, D. D. & Fletcher, R. C. *Fundamentals of Structural Geology* (Cambridge University Press, 2006)
85. Shimizu, H. & Okamoto, A. The roles of fluid transport and surface reaction in reaction-induced fracturing, with implications for the development of mesh textures in serpentinites. *Contrib. Mineral. Petrol.* **171**, 1–18 (2016).

Acknowledgements

We thank Kenichi Hirauchi and Mutsuki Aoya for useful discussions, and Shinichi Yamasaki and Otagongay Dandar for XRF analyses. Fang Huang kindly introduced us to the DEW modeling. Discussion with J.A.D. Connolly helped in clarifying the relation between oxygen fugacity and carbonation reactions. The authors acknowledge constructive comments from two anonymous reviewers that substantially improved this manuscript. This work was financially supported by JSPS KAKENHI Grant Numbers JP16H06347, 18KK0376, and 17H02981 to A.O., and JP15H05831 and 20KK0081 to M.S.-K, and by Earthquake Res. Inst., the University of Tokyo, Joint Research program 2021-B-01 and 2018-B-01.

Author contributions

A.O., R.O., K.Y., and M.U. carried out field work. A.O. carried out the petrological analyses. R.O. carried out the thermodynamic calculations on fluid–rock interaction, M.U. performed mass balance analyses. K.Y. and H.S. developed the DEM model and carried out simulations. M.S. and K.Y. performed the isotope analyses of carbonates. A.O. wrote the paper with inputs from all authors.

Competing interests

The authors declare no competing interests.

Additional information

Supplementary information The online version contains supplementary material available at <https://doi.org/10.1038/s43247-021-00224-5>.

Correspondence and requests for materials should be addressed to A.O.

Peer review information *Communications Earth & Environment* thanks the anonymous reviewers for their contribution to the peer review of this work. Primary Handling Editors: Maria Luce Frezzotti, Joe Aslin, Heike Langenberg.

Reprints and permission information is available at <http://www.nature.com/reprints>

Publisher's note Springer Nature remains neutral with regard to jurisdictional claims in published maps and institutional affiliations.

 **Open Access** This article is licensed under a Creative Commons Attribution 4.0 International License, which permits use, sharing, adaptation, distribution and reproduction in any medium or format, as long as you give appropriate credit to the original author(s) and the source, provide a link to the Creative Commons license, and indicate if changes were made. The images or other third party material in this article are included in the article's Creative Commons license, unless indicated otherwise in a credit line to the material. If material is not included in the article's Creative Commons license and your intended use is not permitted by statutory regulation or exceeds the permitted use, you will need to obtain permission directly from the copyright holder. To view a copy of this license, visit <http://creativecommons.org/licenses/by/4.0/>.

© The Author(s) 2021